ACS OMEGA

Open Access

http://pubs.acs.org/journal/acsodf

Article

Polyfluorinated Naphthalene-bis-hydrazimide for Solution-Grown n-Type Semiconducting Films

Marco Zambra, Vincenzo Mirco Abbinante, Gonzalo García-Espejo, Konstantis F. Konidaris, Pietro Anzini, Candida Pipitone, Francesco Giannici, Mattia Scagliotti, Matteo Rapisarda, Luigi Mariucci, Silvia Milita,* Antonietta Guagliardi,* and Norberto Masciocchi*

Cite This: *ACS Omega* 2023, 8, 43651−43663

Read Online

ACCESS | Metrics & More | Article Recommendations | Supporting Information

ABSTRACT: Naphthalene tetracarboxylic diimides (NDIs), possessing low-lying and tunable LUMO levels, are of wide interest for their aptitude to provide cost-effective, flexible, and environmentally stable n-type organic semiconductors through simple solution processing. NDI-based aromatic hydrazidimides are herein studied in relation to their chemical and environmental stability and as spin-coated stable thin films. In the case of the pentafluorinated residue, these were found to be crystalline, highly oriented, and molecularly flat (roughness = 0.3 nm), based on optical and atomic force microscopy, X-ray diffraction in specular and grazing incidence geometry, and X-ray reflectivity measurements. A new polymorph, previously undetected during the isolation of bulk powders or in their controlled thermal treatments, is found in the thin film and was metrically and structurally characterized from 2D GIWAXS patterns (monoclinic, $P2/c$, a = 17.50; b = 4.56; c = 14.24 Å; β = 84.8°). This new thin-film phase, TF-F5, is formed no matter whether silicon, glass, or polymethylmethacrylate substrates are used, thus opening the way to the preparation of solution-grown flexible semiconducting films. The TF-F5 films exhibit a systematic and rigorous molecular alignment with both orientation and packing favorable to electron mobility (μ = 0.02 $cm^2\ V^{-1}\ s^{-1}$). Structural and morphological differences are deemed responsible for the absence of measurable conductivity in thin films of polyfluorinated analogues bearing $-CF_3$ residues on the hydrazidimide aromatic rings.

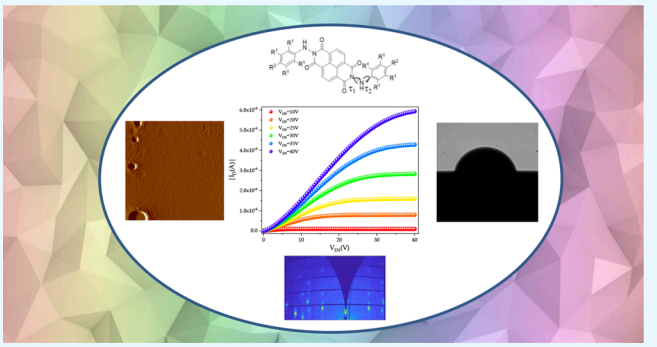

1. INTRODUCTION

The advantages of organic electronics in terms of cost-effective manufacturing, lightweight, printable, and flexible devices have been consolidated by decades of fundamental and experimental studies.[1−7] In this field, a special focus has been dedicated to developing π-conjugated molecular materials of the n-type (electron transporting) class, presently not reaching the level of performance of p-type (hole transporting) semiconductors.[8] In this regard, the bottleneck is the intrinsic poor ambient (air, moisture, heat, and light) stability of n-type semiconductors.[9,10] Additionally, since solution-based deposition methods are the ideal procedures warranting practical fabrication of low-cost electronic devices,[11] several additional aspects such as crystallinity, structure, and morphology[12] of solution-grown thin films remain critical issues.

Thanks to their large electronic affinity (EA), efficient $\pi-\pi$ intermolecular interactions, and easy functionalization, tetracarboxylic aromatic derivatives such as naphthalene dimiide (NDI) and perylene diimide (PDI) have worked as first-class n-type molecular candidates.[8,13−15] Against oxidation, their core functionalization with electron-withdrawing (EW) groups (F, CF_3, Br, and CN) is one of the most effective strategies to raise EA (i.e., lowering the LUMO energy level) above 4.0 eV[16,17] (without exceeding 4.6 eV, to avoid nucleophilic attack or even one-electron reduction[18]). Additionally, efforts have been spent in interpreting and optimizing intermolecular interactions (distance and offset of $\pi-\pi$ stacked aromatic cores) in the solid state,[19−21] as a route to improve the electron mobility,[22] although no definite recipe is to date consolidated. Finally, recent renovated interest in solution-grown (doped) NDI and PDI n-type derivatives is as organic thermoelectrics (O-TE) operating at low-to-medium temperatures (<300 °C),[23−25] an application favored by the low thermal conductivity of organic solids (as required by efficient TE materials). In particular, the thermally or solution-processing-driven polymorphic landscape of NDI/PDI materials adds an undesired variability to their manufacturing and

Received: July 18, 2023
Accepted: September 11, 2023
Published: November 10, 2023

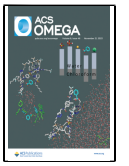

insertion in functional devices. In this respect, in the past, we have studied PDI derivatives with linear[26] and branching[27] side chains to increase molecular solubility thus improving materials processability, while directly influencing the self-assembly and consequently the electrical properties of thin films. We have shown that the disorder generated by the asymmetric branched chains when the molecule is physisorbed in thin films can be instrumental for enhancing charge transport via thermal annealing.[27]

More recently, we have been studying NDI derivatives with a variety of branching "axial" residues and found that NDI derivatives bearing linear $(CH_2)_{(n-1)}CH_3$ residues (n = 4, 6, 8, and 10) manifest an intrinsic and (too) rich polymorphic versatility and a poor control over the crystal structure upon film deposition and processing, attributed to the flexibility of the linear alkyl chains.[28] After replacing the alkyl chains with aryl residues, much higher thermal/polymorphic stability was obtained (above 500 °C, up to melting),[29] at the expense of solubility issues. In the present work, we focus on solution-grown thin films of highly fluorinated NDI dihydrazimides,[30] possessing, at the same time, low LUMO levels (compatible with ambient stability[31]), high thermal and polymorphic stability, and good solution processability. The strategy behind the new derivatives was adding numerous EW groups (F or CF_3 residues) on the aromatic rings in the molecular periphery, boosting the approach already outlined with benzylamine-based NDIs with *single* CF_3, OCF_3, and SCF_3 residues in *para* position, for which significantly improved electron mobility and materials stability are reported.[32,33] Indeed, it is well-known that the high electronegativity and low molar polarization of the fluorinated (F and CF_3-based) groups, often provide, for polyfluorinated species, new and appealing features, such as improved dielectric properties and low moisture uptake.[34] Additionally, the pronounced hydrophobicity granted by fluorinated substituents and the partially inverted charge density distribution in perfluoroaryl rings favor the solubility of these species in comparison to the corresponding hydrocarbons.[35−38] On the other hand, when fluorine atoms bond with carbon atoms, they create a highly stable chemical bond (with ΔH_{diss} up to 540 kJ mol^{-1}).[39] This stability is indeed what gives perfluorinated chemicals their distinct properties, providing strength, resilience, and durability to a variety of products.[40]

The species herein investigated, containing the highly fluorinated 1,4,5,8-naphthalenetetracarboxylic-bis-hydrazimides, are illustrated in Figure 1, where the labeling scheme (F3, F5, F7) recalls the degree of fluorination versus the nonfluorinated precursor (F0). A comprehensive characterization (structural, thermal, polymorphic, and spectroscopic) of the bulk solid materials is presented elsewhere.[30] The first sections of this contribution are dedicated to the spectroscopic characterization of the precursors, complemented by density functional theory (DFT) computational results addressing the LUMO energy variations versus the degree of fluorination and fostering a correct interpretation of the solution UV−vis spectra. We also discuss the outcome of tests on the chemical (redox) stability of the precursors, in solution, prior to film deposition. In the following sections, we present the thin film optimization by spin coating and their morphological (atomic force microscopy - AFM and X-ray reflectivity - XRR data) and structural (specular X-ray diffraction - XRD and synchrotron grazing incidence wide-angle X-ray scattering - GIWAXS) characterization. Highly reproducible preparations of thin films of F5 (20-to-60 nm thick) on a variety of substrates ended up in the formation of a (so far unknown) thin-film phase, exhibiting environmental (chemical and structural) stability over 18 months and thermal stability up to 250 °C. The n-type transport properties of the F5 films were demonstrated by assessing their electrical performances in organic thin film transistor (OTFT) devices, indicating, for a film deposited in the air by spin coating on an unpassivated silicon chip (i.e., without specific precautions), measurable mobility and a time-dependent electrical response in air, which can be recovered by moisture removal in gentle vacuum. Altogether, in this paper, we present and discuss polyfluorinated NDI derivatives, which, though sharing similar chemical and thermal stability, molecular shapes, polarizability, frontier orbitals, and packing features in their solids, do manifest remarkably different performances when deposited as films. Finally, the distinct performances of F5 are interpreted by the serendipitous formation of a new thin-film phase with molecularly flat and extremely oriented slabs of tightly stacked parallel molecules, a feature apparently not shared by F3 and F7 films.

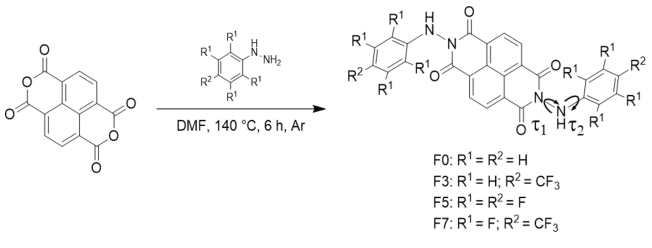

Figure 1. A sketch of the common chemical reaction leading from 1,4,5,8-naphthalene-tetracarboxylic-dianhydride (NDA) to symmetric fluoro-substituted bis-hydrazimides, with the chemical structures of the nonfluorinated (F0) and fluorinated (F3, F5, and F7) molecules. The arrows indicate the τ_1 and τ_2 torsional angles, giving conformational freedom.

2. EXPERIMENTAL SECTION

2.1. Synthesis of Differently Substituted Bis-phenyl-hydrazimides. *2.1.1. Naphthalene-1,4,5,8-tetracarboxyl-bis-phenylhydrazimide (F0).* The synthesis and characterization of F0 species were fully described in a recent paper of ours.[29]

2.1.2. Naphthalene-1,4,5,8-tetracarboxyl-bis-4-(trifluoromethyl)phenylhydrazimide (F3) Naphthalene-1,4,5,8-tetracarboxyl-bis-2,3,4,5,6-pentafluorophenylhydrazimide (F5). F3 and F5 were prepared following a slightly modified protocol than that described in a previously reported procedure.[41,42] Details of the full synthetic procedures, jointly with the NMR, IR, and UV−vis spectral properties, are presented in the Supporting Information file as Supporting Text ST1.

2.1.4. Naphthalene-1,4,5,8-tetracarboxyl-bis-2,3,5,6-tetrafluoro-4-(trifluoromethyl)phenyl-hydrazimide (F7). 2,3,5,6-tetrafluoro-4-(trifluoromethyl)phenylhydrazine (2.22 g, 8.95 mmol, 3 equiv) was added to a mixture containing naphthalene-1,4,5,8-tetracarboxylic dianhydride (0.80 g, 2.98 mmol, 1 equiv) in 40 mL of anhydrous dimethylformamide (DMF) under argon atmosphere. The reaction mixture was stirred at 140 °C for 6 h and then cooled to room temperature. The solution was poured in 150 mL of deionized water and extracted with ethyl acetate. The organic phase was washed with brine solution (4 × 75 mL) and dried over anhydrous

https://doi.org/10.1021/acsomega.3c05172
ACS Omega 2023, 8, 43651−43663

Na_2SO_4 and the solvent was removed under reduced pressure. The crude product was suspended in $CHCl_3$, filtered, and washed with $CHCl_3$. F7 was obtained in 78% yield (1.70 g, 2.34 mmol) as an off-white powder. NMR, IR, and UV−vis spectral properties can be found in the Supporting Information file (Figures S1−S3).

2.2. Redox Stability Tests. The redox chemical stability of the F0−F7 species was tested by comparing UV−vis absorption spectra of their 1,4-dioxane solutions before and after the addition of diluted solutions of H_2O_2 and, separately, of N_2H_4. The molar ratio between each organic species and the oxidizing (H_2O_2) and reducing (N_2H_4) agents was chosen to be 1:2. Based on the UV−vis molar absorption coefficients previously determined for the four investigated NDIs,[25] the prepared solutions (2.3×10^{-5} mol·L^{-1}) showed maximum absorbance values lying in the 0.5−1.5 range. Prior to being analyzed under the UV−vis spectrophotometer, a defined amount of diluted oxidant/reductant solution was added to each of the NDI solutions, and the resulting solutions were stirred for 10 min at room temperature. Further operational details are reported in the Supporting Information file (Supplementary Text ST2, Table S1).

2.3. Computational Analysis. Ab initio DFT was used to describe the ground state (GS) electronic structures on fully relaxed geometries imposing a C_i point group symmetry. The transition energies for electronically excited states were calculated by *ab initio* time-dependent density functional theory (TD-DFT). All the calculations were performed in the gas phase with Gaussian16,[43] using the B3LYP hybrid functional,[44,45] which is widely reported to be a good choice for the description of both ground and excited states in most cases.[46] The 6-31G+(d) basis set was chosen as a compromise between accuracy and calculation time since a preliminary test on F0 confirmed that the TD-DFT results were indistinguishable from 6-31G++(d,p). When discussing the TD-DFT results, the natural transition orbitals (NTOs) were used for a more straightforward depiction of the electronic states involved in the transitions.[47]

2.4. Thin Film Deposition. *F3 films* - Powders of F3 were dissolved in dimethylsulfoxide (DMSO) at 20 mg mL^{-1} concentration. The solution was stirred at room temperature for several hours and then spin-coated at 1700 rpm for 30 s on a SiO_2/Si substrate (50 μL). During an additional 20 s of spin coating, 50 μL of hexane was added as antisolvent. The films were left to dry under a fume hood for 6 h at room temperature. Optical microscopic images indicated the formation of a polycrystalline material with needle-like crystals and an evident surface roughness.

F5 films: Powders of F5 were dissolved in 1,4-dioxane at 10 and 20 mg mL^{-1} concentration. The solution was stirred at room temperature for 24 h under a nitrogen atmosphere and then spin-coated at 2000 rpm for 15 s on a SiO_2/Si substrate. The films were annealed at 120 °C for 30 min to ensure the complete solvent removal.

F7 films: Powders of F7 were dissolved in 1,4-dioxane at 20 mg mL^{-1} concentration. The solution was stirred at room temperature for several hours and then spin-coated at 2000 rpm for 15 s on a SiO_2/Si substrate (80 μL). The films were left to dry under a fume hood for 6 h at room temperature. Microscopic images indicated that the film was rather homogeneous, but, using XRD, we could not detect any Bragg peak, but only Kiessig fringes (indicating a ∼50 nm film thickness, see Figure S4). Low-T annealing (<90 °C) clearly destroyed film homogeneity, as witnessed by the appearance of tiny crystals and large inhomogeneous spots due to material dewetting. In both F3 and F7 cases, changing the solvent and deposition parameters did not improve the film quality.

2.5. Thin Film Characterization. *2.5.1. Morphological Characterization.* The morphology of the thin films was studied by collecting AFM images in noncontact mode on a psia XE100 system, in air, and at room temperature. The image analysis was performed using Park Systems XEI 4.3.4 and Gwyddion 2.57 software.

2.5.2. Determination of Hydrophobicity. Thirty microliters drops of deionized water were deposited on the top of pressed pellets of F0, F3, F5, and F7 powders, as well as on thin films of the polyfluorinated systems. Images of transmitted white light (collected in Figure S5) were taken on a homemade instrument inspired by that illustrated by Lamour et al.[48] and were analyzed by the ImageJ LB-ADSA plugin.[49]

2.5.3. X-ray Films Characterization. 2D-GIWAXS images were collected at the XRD1 beamline of the ELETTRA synchrotron radiation facility in Trieste (Italy). A Pilatus 2 M silicon pixel X-ray detector (DECTRIS Ltd., Baden, Switzerland) was positioned perpendicular to the incident beam 250 mm away from the sample (λ = 1.50 Å and beam size of 200 × 200 μm^2). Two different X-ray beam grazing incident angles were chosen: (i) α_i = 0.15°, probing the uppermost film layers (the X-ray penetration depth is ∼4 nm) and (ii) α_i = 0.25, probing the full film thickness. The visualization and analysis of the recorded 2D-GIWAXS images were performed using the open software GIDVis suite of programs.[50]

Specular XRR and XRD measurements were performed by using a SmartLab−Rigaku diffractometer equipped with a rotating anode source (Cu K_α, λ= 1.5418 Å), a parabolic mirror collimating the incident beam, and a series of variable aperture slits (placed in the primary and diffracted beams). XRR data were analyzed through the GXRR software package,[51] enabling the determination of film thickness and roughness. Raw GIWAXS images of F3 and F7 films and their derived 1D powder plots obtained by azimuthal integration are reported in the Supporting Information (Figure S6), together with the lattice parameters derived therefrom.

2.5.4. Ab Initio Structural Characterization of the Thin-Film Phase of F5. Unit cell determination of the thin-film phase of F5 was performed using GIDInd, which provided an initial triclinic cell with a = 17.78, b = 4.56, c = 14.49 Å, α = 91.5, β = 84.5, and γ = 88.5°; V = 1169 Å^3, Z = 2 and dq_{xyz} = 0.015 Å^{-1}.[52] Figure S7 shows the indexed GIWAXS image. Further analysis provided a monoclinic symmetry, with $\alpha = \gamma$ = 90° and slightly modified a and c axes (a = 17.50; b = 4.56; c = 14.24 Å; β = 84.8°). The approximate structural model of this phase was initially obtained by using (in Pc, in line with systematic absences) an entire rigid F5 molecule, defined by the z-matrix algorithm with standard bond distances and angles and flexible at the four N−N and N−C exocyclic hinges (τ_1 and τ_2 of Figure 1, 2×). Using TOPAS-R in the *only penalties* mode,[53] the molecule was oriented in crystal space by imposing *antibump* restraints among non-H atoms in the form of a threshold of 3.2 Å. The symmetry rises to $P2/c$ (by imposing a semiquantitative match of the intensities of the h00 peaks in the highly textured specular XRD trace) immediately followed.

2.5.5. OTFT Device Fabrication. Bottom Gate/Top Contact (BGTC) organic thin-film transistors (OTFTs)[54] were fabricated by using a heavily doped Si wafer (gate), having a

https://doi.org/10.1021/acsomega.3c05172
ACS Omega 2023, 8, 43651−43663

100-nm thick thermal SiO_2 layer as dielectric. Source (S) and Drain (D) Au electrodes (L = 50 μm, W = 1 mm and 30 nm thick) have been evaporated in high vacuum (HV) conditions, through a metal shadow mask positioned directly on top of the organic semiconductor film. The whole fabrication process was carried out in a cleanroom environment at a low temperature (<150 °C), in air, with no need for glovebox-controlled environment process steps. Following the above-mentioned specifications, the process is compatible with large-area flexible organic electronics,[55,56] allowing a fast, simple, and clean process,[57] but, as later substantiated in Section 3.7, might require film encapsulation and/or a slightly different (and optimized) BGTC architecture for improved electrical performances.

2.5.6. OTFT Electrical Characterization. The transfer (I_{DS} vs V_{GS}) and output (I_{DS} vs V_{DS}) curves were measured in a low vacuum environment, using an MMR variable temperature microprobe system connected to a Keithley 236 and a Keithley 2635 source/meter units. The charge transfer experiments have been carried out in linear and saturation transistor regimes, i.e., at V_{DS} = 1 V and V_{DS} = 40 V, respectively, in up−down mode, by sequentially sweeping the gate voltage, V_{GS}, from off-to-on (onward scan, from −10 to 40 V) and from on-to-off (backward scan, from 40 to −10 V). The output characteristics have been recorded for the 10 < V_{GS} < 40 V range.

3. RESULTS AND DISCUSSION

3.1. Synthesis and Chemical and Environmental Stability. The synthetic path used for the preparation and isolation of the F0−F7 species is presented in Figure 1. Compared to similar reactions reported in the scientific literature,[41,42,58] the most relevant changes can be traced in the work-up procedure of species F3 in which the crude product is slurried in $CHCl_3$ and then filtered, obtaining quantitative yields (to be compared to the <77% values reported in the original paper).[41,42] The same synthetic strategy was also followed when preparing F7. In this way, for both F3 and F7, 100% pure crystal phases were isolated, and the reported formation of the tetrahydrofuran (THF) solvate, obtained from the recrystallization of F3 in THF,[42] is easily avoided. Additionally, by limiting the amount of THF during the precipitation/purification steps, F5 was also obtained in a much higher yield (83% vs <55%[41,42]), when the crude product was dissolved in a minimal amount of hot THF (60 °C) and then precipitated by adding cold water.

The chemical stability of F0−F7 molecules was tested by reacting them in a 1,4-dioxane solution with (reducing) aqueous N_2H_4, and separately, with (oxidizing) aqueous H_2O_2. Hydrazine, which has negative standard reduction potentials in the entire pH (0 to 14) range, is a strong reducing agent, while H_2O_2 can act both as a strong oxidant ($E°$ = 1.35 V at pH = 7) and as a reducing agent. Thus, both N_2H_4 and H_2O_2 species were used as testing agents to probe molecular stability, with the obvious caveat that, for n-type semiconductors, resistance to environmental oxidation is far more important. In both cases, the UV−vis absorption spectra did not change with respect to those of the pristine solutions, demonstrating the endurance of these phases to harsh oxidizing or reducing conditions (see Figure S1). As reported by Gostzola et al.,[59] upon progressive (electrochemically induced) formation of NDI-reduced species (a $R^{\bullet-}$ radical anion or a R^{2-} dianion), absorption peaks redshift by 50 nm or more, and enter the visible range, an occurrence that was not observed in our experiments. The quantitative one-electron reduction is expected at potentials ideally above the standard reduction potential of hydrazine (−0.75 V vs NHE in water at a neutral pH). This is evident for PDI-substituted diimides, with reported $E_{1/2}$ values (determined from solution cyclovoltammetric studies) falling near −0.10 V or above,[60] for LUMO levels near −4.5 eV. A further confirmation of the redox stability of our compounds is provided by our computational study (discussed in the following section) performed on the entire F3, F5, and F7 series. Their (gas-phase) LUMO levels are significantly lower than that of F0 (−3.98 eV) and lie slightly above the −4.4 eV threshold, a value associated with ambient stability in favor of the use of these molecules as air-stable organic semiconductors.[61] However, our calculated values, jointly with those reported from cyclovoltammetric estimates in solution (e.g., for F0, −3.98 (see below) and −4.01 eV, respectively[25]), suggest a lower reduction propensity of the fluorinated naphthalene-bis-hydrazimides than in (bisalkyl)-PDI-based systems, which, therefore, remain the best performers.

The environmental stability for powders left in air for several months was also monitored, with no evident changes of their XRD trace being observed over an 18-month period. This resistance against moisture is also supported by the noteworthy hydrophobicity exhibited by the surfaces of these materials, as proved by contact angle measurements (images are shown in Figure S5), revealing a ca. 70° value (reference values, experimentally determined on ordinary glass and Teflon, being ca. 20° and 140°, respectively). These values compare well with those observed for water droplets deposited on a number of hydrophobic organic polymers, such as polylactic acid or polymethylmethacrylate.[62] We also tested the behavior of F3, F5, and F7 thin films and found slightly larger contact angles, possibly attributed to the lower amount in the films of environmental moisture that can partially fill the intergrain voids in porous solid pellets. However, the effect of exposing films of F5 to aerial moisture (which can be reversibly eliminated by vacuum or heating treatments) has been found detrimental to electrical performances but not to structural and compositional film stability and is discussed in Section 3.7.

3.2. Computational Analysis. Table 1 presents the GS energies of the frontier molecular orbitals of F0, F3, F5, and F7

Table 1. Energy Level of the Frontier Orbitals (HOMO and LUMO Calculated with the Two Methods Described in the Text), the Calculated Wavelength of the Two Main Transitions in the UV/vis Range (λ_1 and λ_2), and Their Oscillator Strength (f_1 and f_2)

species	HOMO, eV	LUMO, eV method 1	LUMO, eV method 2	λ_1, nm	λ_2, nm	f_1	f_2
F0	−6.26	−3.98	−4.59	375	358	0.35	0.08
F3	−6.80	−4.27	−5.18	375	336	0.39	0.08
F5	−7.07	−4.22	−5.52	375	340	0.39	0.03
F7	−7.54	−4.37	−5.69	374	339	0.42	0.04

(reported in ref 30). As per Koopmans' theorem (valid for perylene diimide compounds),[63] these GS energies represent the first ionization potential (defined as −HOMO energy) and the electron affinity (defined as −LUMO energy) of the isolated molecules. Following the theorem approach (hereafter called method 1), the LUMO energy was calculated from the

https://doi.org/10.1021/acsomega.3c05172
ACS Omega 2023, 8, 43651−43663

singlet GS. These "method 1" values should be taken in comparison with those determined for a bevy of NDI derivatives appearing in the pertinent literature.[8] The large collection of LUMO energies gathered by Shukla et al. acts as a very significant reference;[64] calculated by similar computational approach(es), these values manifest that, in the absence of extensive core substitution by EW groups or of fused (hetero)aromatic rings, LUMO levels of *axially* substituted NDIs[64] never overcome the −4.0 eV threshold. As reported in Table 1, (poly)fluorination in F3, F5, and F7 efficiently lowers LUMO energies down to −4.37 eV for F7.

However, a better approximation of the LUMO energy is described by McCormick et al. that gives a substantially improved match with experimental data.[65] The triplet electronic state is computed (i.e., one electron in the former HOMO and one in the former LUMO, both with the same spin), and the energy of the highest singly occupied MO of the triplet state is taken as the LUMO energy (here, method 2). A much clearer trend of lower (more negative) LUMO energy values with increasing fluorination is obtained with method 2 (Table 1) that parallels that of lower HOMO energies. The conceptual shortcoming of identifying the HOMO and LUMO energy levels from DFT as ionization potential and electron affinity is widely recognized;[66] however, it is also balanced by a multitude of cases where ab initio modeling is able to rationalize the observed trends in redox potentials and optical gaps.[8,67]

The vertical optical transition energies and intensities (from the singlet GS to the singlet excited state with the same geometry) were calculated with TD-DFT and are shown in Table 1. In addition, since all structures have an inversion center and the GS symmetry is A_g, all optically allowed transitions have A_u symmetry (i.e., A_g transitions are forbidden according to the so-called Laporte rule). In particular, the HOMO → LUMO transition, estimated to fall around 1.7 eV (700 nm), is forbidden (oscillator strength less than 10^{-4}), while the most intense transition is found to have a photon energy of 3.3 eV (maximum absorbance at 375 nm, λ_1 in Table 1) for all compounds, in rather good agreement with the solution-based absorption spectra supplied in Figure S1. The NTO analysis shows that the most intense transition (λ_1 in Table 1) can be described mainly as a HOMO−4 → LUMO: both these orbitals are placed on the polyaromatic core, corroborating the observation that λ_1 hardly changes in the whole series. Likely, this transition is also responsible for the absorption coefficient rise in the (solid-state measured) Tauc plots, as the associated photon energies reasonably agree with the experimentally determined optical E_{gap} values (2.8−2.9 eV) and with their limited dependence on side-chain substitution.[30]

Another less intense transition (λ_2 in Table 1) is predicted but has a different character throughout the whole series: HOMO → LUMO+1 in F0 and F3, HOMO−6 → LUMO in F5, and HOMO−4 → LUMO+2 in F7. In the NTO description, the particle density (i.e., the HOMO in a simplified picture) is substantially located on the branching arylhydrazides and induces an evident shift in the corresponding wavelength (λ_2) when the fluorination level is changed. It is worth mentioning that some approximations were made in our calculations: (i) we neglected all intermolecular interactions (present in the solid-state), which, in crystalline PDI analogues, were shown to lead to 0.5−1 eV broad valence bandwidths.[63] (ii) We optimized the dihedral angle between the NDI core and the fluorinated rings for individual gas-phase (and centrosymmetrical) molecules, though the molecular conformation in the solid state (affected by the crystal packing environment) might be slightly different. In this regard, our X-ray refined[30] and computationally optimized values for the τ_1 and τ_2 torsions (illustrated in Figure 1) show similar values (with maximum and average differences of 15.5° and 8.9°, respectively), thus making most of the possible absolute changes between gas-phase and solid-state frontier orbital energies attributable to crystal packing and transfer integral effects. Similarly, Brédas et al. nicely emphasized that, for the PDI congeners, "molecular packing, through band narrowing or widening, also impacts the transport levels to an extent that is far greater than intramolecular functionalization does".[63]

3.3. Film Preparation and Characterization. Solution-grown organic semiconductor films are considered effective alternatives to the time-consuming and expensive sublimation procedures, as long as the materials can be solubilized in organic solvents that are compatible with the substrate on which they are spin-coated or drop-casted. The solubility of many of the systems herein investigated was previously tested in several common organic solvents. Specifically, using a set of 10 common organic solvents and limiting, as an arbitrary operational threshold of 2 mg mL^{-1} for considering an NDI derivative sufficiently soluble for efficient spin-coating film deposition, the fluorinated species were found to be soluble in three, six, and five cases, respectively (reaching values as high as 40 mg mL^{-1}).[30] At variance, F0 proved to be soluble only in DMF (40 mg mL^{-1}) and, to a much more limited extent (4 mg mL^{-1}), in THF. Additional tests performed of the non-fluorinated *p*-aminophenyl-derivative characterized by us in 2021[29] showed a maximum solubility of 1 mg mL^{-1}, well below any practical use. On the basis of these tests, 1,4-dioxane, DMF, and DMSO were chosen as the most practical solvents, and films of the F3, F5, and F7 species were prepared by spin coating onto three different substrates: monocrystalline silicon, quartz, and glass plates. In spite of the large series of concentrations and operational conditions tested (spinning rate, duration, and amount of liquid), the thin films of F3 and F7 revealed scarce reproducibility, both structurally and morphologically. Figure S4 shows conventional XRPD traces for highly oriented polycrystalline F3 films deposited from DMF solution (needles on Si/SiO_2 substrate) and amorphous F7 films from 1,4-dioxane (50 nm thick, with evident Kiessig fringes without annealing). At variance, (annealed) films of F3 from acetone and F7 from 1,4-dioxane provided GIWAXS images displaying continuous (but partially textured) "powder-like" Debye−Scherrer rings, belonging to polymorphs different from those structurally characterized in powder form (see Figure S6).

Although the lattice metrics of a new thin-film polymorph of F3 (Orthorhombic P, details in Figure S6) could be derived, its detailed crystal structure remains uncharacterized due to the paucity of detectable peaks and their extreme overlap. For F7, the GIWAXS image and the corresponding 1D powder plot were attributed to the RT version of the high-temperature phase measured in the bulk at 310 °C.[30] Also this phase (*β*-F7) is Monoclinic C, with relatively large unit cell parameters, and remains structurally unknown.

Based on the unsuitable structural and morphological features, F3 and F7 were not deeply characterized in the form of thin films. We then tackled a much deeper investigation of the films of F5 and additional discussion on

https://doi.org/10.1021/acsomega.3c05172
ACS Omega 2023, 8, 43651−43663

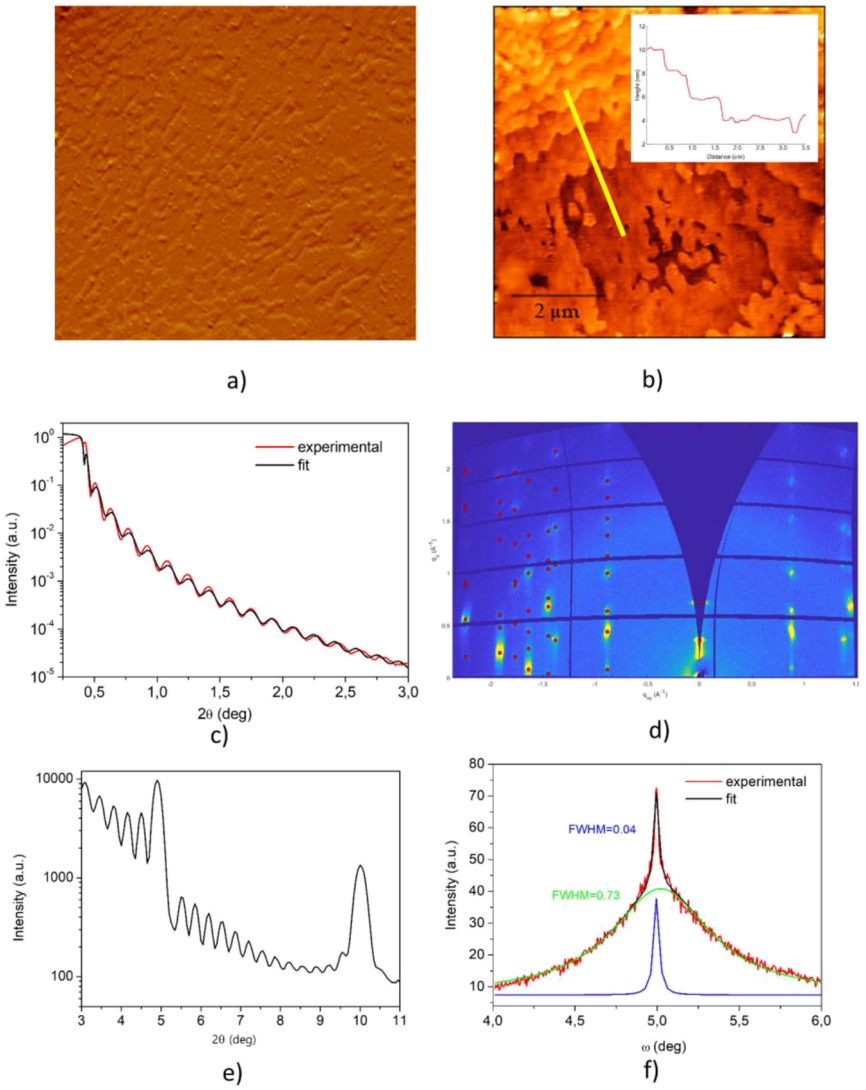

Figure 2. For a 50 nm-thick film of F5, deposited on SiO_2/Si substrate: (a, b) AFM images; the inset in (b) represents the height profile of the yellow line in the main panel, (c) XRR experimental (red) and model (black) curves (log scale), (d) 2D-GIWAXS image, with indexed peak positions, (e) specular XRD pattern demonstrating the presence of many Laue fringes (log-scale), and (f) 200 rocking curve (red) with the Gaussian fit (black), with the contribution of two components drawn by the blue and green traces.

possible reasons impeding beneficial film morphology for the other (F3 and F7) species is later discussed.

3.4. F5 Film Preparation and Characterization. Depending on the concentration of the starting F5 solution (10 or 20 mg mL^{-1}), thinner (ca. 25 nm) or thicker (ca. 50 nm) films have been deposited by spin coating on a SiO_2/Si substrate. Film thickness is highly reproducible with atomic precision, as tested through four distinct preparations for each nominal concentration (5, 10, and 20 mg mL^{-1}), ending up with uniform values of 10.3(3), 25.5(5), and 51.1(9) nm. This result indicates that the thickness of the films depends linearly on concentration (all other conditions being kept unchanged) while more concentrated solutions provide an expected leveling (see Figure S8). Additionally, regardless of their thickness, all investigated F5 films exhibit the same morphological and structural features. AFM images of a typical film spin-coated on a SiO_2/Si substrate show a homogeneous and flat surface (Figure 2a). A topographic image (Figure 2b) in a defective zone of the surface highlights the occurrence of a terraced texture composed of molecular layers with ca. 2 nm steps (z-profiles are shown in the inset of Figure 2b and in Figure S9). In line with these observations, XRR profiles indicate a highly homogeneous film surface (1.0 cm^2 wide) with a very limited roughness (ca. 0.3 nm) for a film thickness of 51.4 nm, as per the fit procedure reproducing the experimental curve in Figure 2c.

Such nearly null film roughness and its persistence for all the investigated films of F5 have been reported for few solution-processed highly oriented organic films, such as BASF's N1400 species, a branched PDI derivative.[27] This is an additional proof of the 2D arrangement of the organic molecules on the substrate, which is considered crucial in determining their charge transport properties.[68]

The specular XRD measurements provided information about the molecular arrangement in the film system (see Figure 2e). The few recorded peaks can be indexed as $h00$ reflections, with $d_{h00} = 17.4/h$ Å, roughly matching the 2 nm monolayer thickness observed by AFM. This result suggests that F5 molecules provide 2 nm-thick lamellae where stacking of the NDI core extends parallel to the substrate plane. Laue

https://doi.org/10.1021/acsomega.3c05172
ACS Omega 2023, 8, 43651−43663

Table 2. Crystal Data for the Thin-Film and the Other Known Polymorphic Forms of F5[30a]

species	system	space group	*a*, Å	*b*, Å	*c*, Å	*α*, °	*β*, °	*γ*, °	*V*, Å^3	Z	*ρ*, g cm^{-3}
TF-F5	monoclinic	$P2/c$	17.50	4.56	14.24	90	84.8	90	1132	2	1.841
α-F5	monoclinic	$P2_1/n$	17.35	5.30	12.12	90	87.6	90	1112	2	1.876
γ-F5 (310 °C)	monoclinic	$P2_1/n$	30.49	7.72	4.99	90	89.2	90	1175	2	1.775
ω-F5	monoclinic	$P2_1/n$	21.50	10.58	4.96	90	86.6	90	1127	2	1.851

[a]Values in italics refer to the stacking vector length within each column of *π*−*π* stacked NDI molecular cores.

oscillations around the 100 peak (see Figure 2e) were observed for all of the samples, highlighting the structural coherence along the depth profile and indicating a persistent ordered molecular arrangement throughout the entire film.

The 200 rocking curves (*ω* scans, shown in Figure 2f) enabled the extraction of additional information from the peak width, measuring the film mosaicity (the angular spread of the orientations of the crystallites). These profiles indicate the simultaneous presence of a sharp and a broad crystallite distribution, resulting in two peaks (0.04° and 0.73° wide, respectively) corresponding to a highly textured fraction to a less textured one.

Worthy of note, these F5 films were found indefinitely stable (over 18 months), as witnessed by highly reproducible XRD measurements performed on samples stored in air at room temperature, under environmental moisture and light conditions. Figure S10 shows the XRD data repeatedly collected within 12 months of the original film deposition.

The 2D-GIWAXS images (Figure 2d) witness the high crystallinity and the pronounced texturing of the films: the spot shape of the diffraction signals together with their symmetric distribution around the vertical direction (q_z) allows fiber texturing of the crystallites to be established. Remarkably, the data indicate the presence of a new thin-film polymorph, here labeled TF-F5, distinct from that of the room-temperature isolated powder, and from the *β*, *γ* and *ω* polymorphs of F5, obtained by (or after) high-temperature treatments (well above 250 °C). The crystal and molecular structures of TF-F5 are described in detail in Section 3.5.

Finally, the same crystalline TF-F5 phase observed on silicon and glass is obtained by spin-coating F5 onto a 50−60 nm thick polymethylmethacrylate (PMMA), indicating easy reproducibility on flexible substrates, also supported by the wide-angle XRD region data fully consistent with those of the original Si/SiO$_2$ − deposited F5 data (Figure S11).

3.5. The Crystal and Molecular Structure of the TF-F5 Polymorph. *Ab initio* peak indexing/cell determination enabled the extraction of the lattice parameters of FT-F5 (here, monoclinic), compared in Table 2 with those of the *α*-, *γ*-, and *ω*-F5 crystal phases.

Through simulated annealing techniques and a rough geometrically constrained optimization of the molecular location, orientation, and conformation, the shape and position of the F5 molecules within the TF-F5 lattice were determined (see Experimental Section for details). The atomic coordinates are supplied in Supporting Information Table ST2. Figure S12 further compares the observed XRPD pattern of a 100% *h*00-oriented film with that computed from the TF-F5 structural model by applying a March-Dollase factor r_{h00} = 0.2.[69]

Despite the close similarity of the crystal metrics of *α*-F5 and TF-F5, the two polymorphs are different. Analogies and differences are easily caught in Figure 3 that shows the crystal packings in a comparative way. With equioriented cell axes and *π*−*π* contacts running normally to the images, heavily

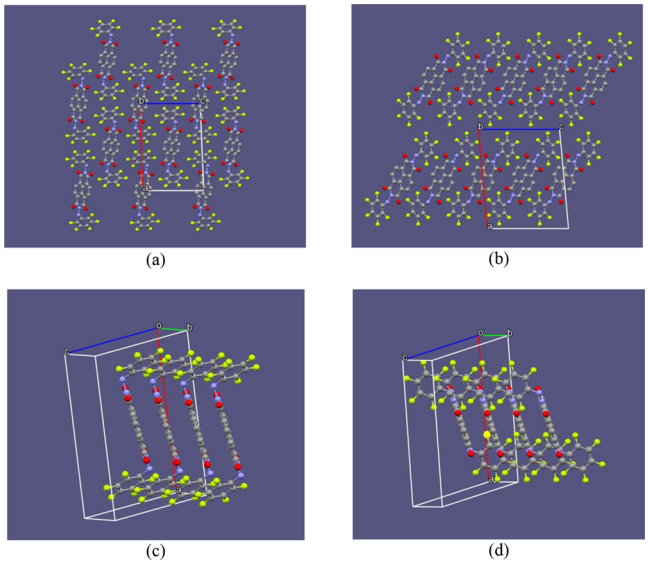

Figure 3. Crystal packing of *α*-F5 (a) and TF-F5 (b), view down [010], with equioriented cell axes. In both cases, the *π*−*π* stacking (dictated by the short **b** axis, see Table 2) runs normal to the images. While interdigitated F5 molecules are present in *α*-F5, 2D slabs, stacked along **a***, can be easily envisaged in the structure of the thin films. In panels (c) and (d), the directions of the *π*−*π* stacking are highlighted. Hydrogen atoms have been omitted for clarity.

interdigitated F5 molecules are visible in *α*-F5 (Figure 3a), while 2D slabs stacked along the **a** direction are present in the TF-F5 structure (Figure 3b). This structural feature can be considered to be responsible for the very flat surface of the films (as indicated by XRR measurements) and for the occurrence of ca. 2 nm steps (evidenced by AFM *z*-profiling). The formation of the new TF-F5 phase, its morphology and orientation, with the *π*−*π* conductive path lying parallel to the substrate, was then considered as promising factors toward enhanced electron mobility in the film.

To further deepen our comprehension of TF-F5, we studied the progressive formation of the crystalline film on the SiO$_2$/Si substrate by in situ XRD measurements performed during the film heating. In the range between 30 and 100 °C, only Kiessig fringes, attributed to a ca. 26 nm-thick film, are observed (see Figure 4a). At higher annealing temperatures, from 110 to 230 °C, the 100 and 200 peaks of the TF-F5 crystal phase clearly emerge, which disappear above 250 °C, as the material progressively sublimes without transforming into any of the known *α*-, *β*-, *γ*-, or *ω*-F5 phases. The Kiessig fringes persist until sublimation; their position and separation are slightly different than those below 110 °C, witnessing a slight shrinking of the film thickness by ca. 1 nm, which we attribute to residual solvent desorption (see Figure 4b). In the 110−230 °C range, a linear expansion of the film, normal to the substrate surface, is observed, with a thermal strain coefficient κ_{100} of 72 × 10^{-6} K^{-1}, 3.5 times larger than κ_a in *α*-F5 (see Figure 4c). This

https://doi.org/10.1021/acsomega.3c05172
ACS Omega 2023, 8, 43651−43663

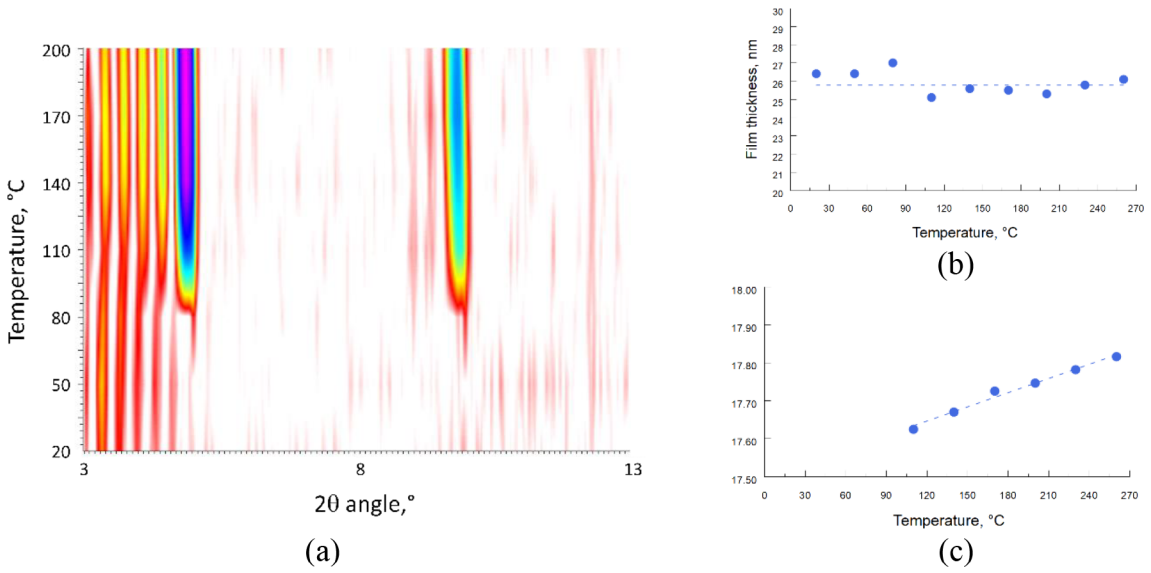

Figure 4. In panel (a), the evolution of the low-angle scattering trace upon increasing the temperature of a 26-nm-thick TF-F5 (intensities are plotted in log scale). Below $2\theta = 5°$, periodic Kiessig fringes are present at all temperatures, while the two strong Bragg peaks (falling near 5° and 10° 2θ) only appear at 110 °C and above. In (b) and (c), the corresponding changes of the film thickness and the d_{100} value, respectively.

observation is in line with a larger inertness of the latter in the presence of interdigitated moieties and likely with its lower (more negative) formation enthalpy, as also suggested by the slightly higher (by 1.7%) density value (see Table 2).

3.6. The Crystal Phase Composition of the Sublimed Films. The GIWAXS experiments, performed at RT on a sublimed film, suggested the formation of a polycrystalline mixture, made by separate crystals of the previously discussed TF-F5 thin film phase and of another crystal phase, soon recognized to be γ-F5 (with cell parameters slightly contracted—as expected—from those measured at 310 °C[30]). The GIWAXS image and the full indexing are shown in Figure S7b. Images collected at different grazing incidence angles (α_i from 0.05 to 0.20°) showed no variations, thus witnessing the substantial compositional homogeneity normal to the film substrate. Figure S13 shows, side by side, the packing diagram of these phases, which clearly demonstrates the formation of two distinct crystalline environments and symmetry but the occurrence of similar stacking (along **a***) of ordered slabs less than 2 nm thick. Simplifying, in TF-F5 the slabs stack by a simple translation (the **a** axis) in an ···AAAA··· sequence, while in γ-F5 the presence of a 2-fold screw axis parallel to **b** generates antiparallel slabs, stacked along **a*** in an ···ABAB··· fashion. Both of these structures are clearly distinct from the starting α-F5 material, characterized by interdigitated molecules (as per Figure 3a). Therefore, we can safely conclude that both spin-coating and sublimation methods on SiO_2/Si substrates provide highly oriented h00 films, but due to the polyphasic nature of the latter, their further characterization was abandoned.

3.7. Charge Transport Properties. Since in our measurements, we employed the staggered (BGTC) configuration, contact effects are strongly reduced, allowing the transport properties of the organic semiconductor to be properly inferred from the electrical characteristics of organic devices.[70,71] The whole fabrication process, carried out in a cleanroom environment at low temperature (<150 °C), is compatible with large area flexible organic electronics[55,72] and allows a fast, simple, and clean process.[73] Typical up—down transfer characteristics of the OTFT device prepared by solution processing of F5 (see Experimental Section) are shown in Figure 5 in both linear and log scales for two (linear and saturated) transistor regimes (V_{DS} = 1 and V_{DS} = 40 V, respectively). Considering the maximum of the transconductance relative to the off-to-on curve for V_{DS} = 1 V[74] of Figure 5b, the calculated field-effect mobility is μ_{FE} = 0.02 cm^2 V^{-1} s^{-1} (slightly better than Katz's fluoroalkyl-substituted NDIs measured in air[75]). In TF-F5 films, the on—off ratio is about 10^4 and the threshold voltage V_{TH} and the subthreshold slope SS are −10.1 V and 1.1 V/dec, respectively. Note that the carrier mobility value of TF-F5, far from being exceptional, falls above the normal range found for axially substituted NDI derivatives (10^{-4} cm^2 V^{-1} s^{-1}, see the compilation present in ref 76), whereas higher mobility values (up to 2 cm^2 V^{-1} s^{-1}) were obtained in bay-fused aromatic moieties (see, e.g., compound 95 presented in ref 64). For a solution-processed film of this type and in the absence of specific precautions, this is considered appreciable[75] and points to higher values for proper process optimization, e.g., after insertion of self-assembled monolayers in the BGTC architecture.[77]

The high quality of the morphological and structural properties of F5 thin films and their nonnegligible electrical performances are expected to be useful for several applications in the microelectronics and sensing fields, where readable conductivity values are requested. The current flowing in F5 films in a transistor structure at a predetermined voltage has been measured, leading to a conductivity value of 7.2 × 10^{-4} S/m, not too far from that of undoped silicon (4.1 × 10^{-4} S/m[78]).

To further test the stability of the synthesized material and of the fabricated devices, we also analyzed the electrical transfer characteristics of an OTFT in different environments. Details of the experiments and of the relevant results are reported in the ESI (Figure S14 and Supplementary Text ST3). Suffice here to say that the electrical characteristics remain stable after several months of storing the devices in a vacuum, while, when the measurements are carried out in air, an increase in the hysteresis between the up and down curves

https://doi.org/10.1021/acsomega.3c05172
ACS Omega 2023, 8, 43651−43663

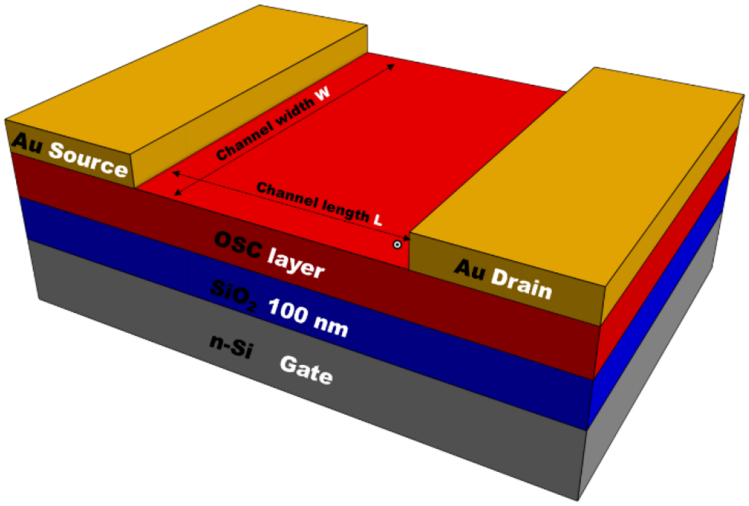

(a)

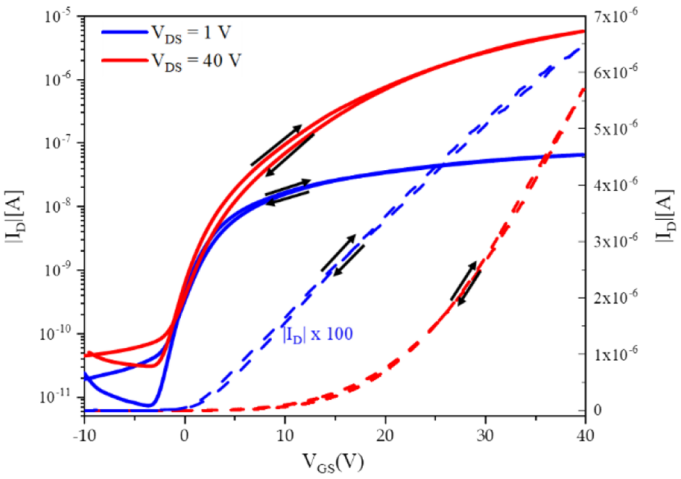

(b)

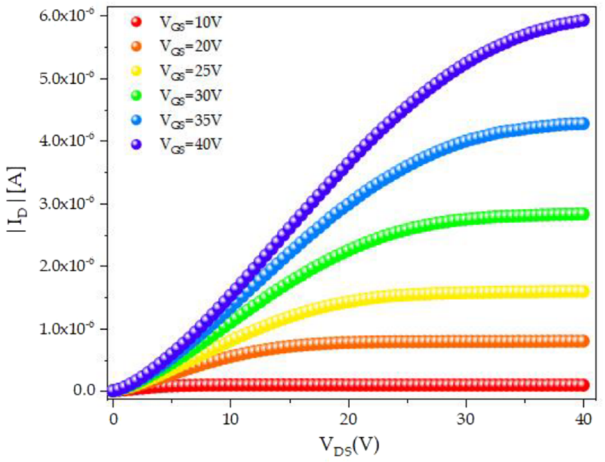

(c)

Figure 5. (a) 3D device schematics. The test structure is in BGTC configuration. (b) Transfer characteristics I_D vs V_{GS} of the F5-based OTFT in log (solid lines, left scale) and linear (dashed lines, right scale) representations, for V_{DS} = 1 V (blue lines) and for V_{DS} = 40 V (red lines). The blue dashed line represents $I_D \times 100$, for better plot visualization; (c) Output characteristics of the OTFT device, measured at different V_{GS} voltages.

(Figure S14a) appears, causing a decrease in the field-effect mobility (Figure S14c). Such hysteresis is related to the absorption of water in the semiconductor layer and/or at the interface with the dielectric and it is not an indication of degradation of semiconductor properties.[79] Indeed, if the sample is put back in a vacuum after short air exposure, the characteristic recovers the initial values. The evolution in time (for a total of ca. 150 h of film exposure to environmental conditions) was also studied and a progressive (asymptotic) deterioration of the film performances was observed, with an increase of hysteresis and a reduction of the field-effect mobility (Figure S14c). However, the OTFT characteristics rapidly restore their initial values by annealing the device at 100 °C (Figure S14d). This instability can be efficiently prevented by the use of an appropriate encapsulation layer,[80] often essential for protecting organic semiconductor devices, like the OTFTs.[79,81]

We also performed a parallel study on the F3 and F7 films, but the drain current was not modulated by the voltage applied to the gate electrode, and no measurable current was detected in the whole measurement range (V_{GS} = −20 to +40 V, V_{DS} = 40 V). We attribute this failure to the unsuitable film morphology and lack of highly textured samples of F3 and F7 crystal phases. In search of a qualitative explanation of this finding, we note the presence of the *p*-CF_3 residue, which has markedly different Hammett's σ and molar refractivity values than a single fluorine atom in F5,[82] together with its possible rotor dynamics. Apparently, this is detrimental to the formation of stacked layers separated by face-to-face $-CF_3\cdots F_3C-$ intermolecular contacts.

https://doi.org/10.1021/acsomega.3c05172
ACS Omega 2023, 8, 43651−43663

Summarizing, after having studied a number of cases,[28−30] we can draw some interesting conclusions: (i) disubstituted NDI systems bearing flexible alkyl residues are soluble and filmable but, due to their high conformational freedom, show many polymorphic phases in a relatively low-temperature regime and, therefore, are of little use. (ii) Rigid residues of the aromatic type reduce material solubility and prevent thin film deposition by solution processing (either drop casting or spin coating). (iii) Polyfluorinated aryls show greatly enhanced solubility and may, or may not, align properly as a lamellar structure on the surface of flat substrates. The further observation that, in both electrically silent F3 and F7 phases, protruding *p*-CF_3 residues disfavor the formation of a semiconducting phase, is an appealing hypothesis, which, however, appears to be dismissed by Katz's (air-stable) trifluoromethylbenzyl NDI derivative, crystallizing in a *herringbone* structure and showing a charge mobility μ = 0.43 $cm^2\ V^{-1}\ s^{-1}$.[32]

4. CONCLUSIONS

N-substituted NDI organic semiconductors bearing polyfluorinated aromatic residues have been prepared in the form of thin films. Solubility properties, chemical stability in environmental conditions, and even harsh treatments with strong oxidizing and reducing agents proved their suitability as stable materials for solution-based film deposition processes. One of these species, the pentafluorinated hydrazidimide (F5), was reproducibly prepared as thin (<60 nm), flat, and homogeneous films with highly controllable thickness depending on the concentration of the starting solution. By synchrotron X-ray GIWAXS analysis, it was found to crystallize in a newly detected polymorphic crystal phase. This form systematically offers a rigorous alignment on silicon or glass substrates, with a molecular orientation and packing favorable to charge mobility, measured by electric transport features in OTFT devices. This orientation is also maintained when deposited by conventional solution-based spin-coating methods on a 50-nm PMMA film, opening the way to its use in flexible electronics. These films are environmentally stable for at least for 18 months and thermally stable up to 250 °C, as long as their composition and structure are concerned, but suffer a fast deterioration of their electrical performances in the presence of moisture. Vacuum pumping or thermal treatments can reversibly restore the initial performance levels. Worthy of note, the n-type semiconductor properties of F5 were determined on films deposited *from solution in air* (that is, in the easiest and cheapest conditions available). Though it is well-known that the introduction of interface layers can lead to a change in the morphology and structure of the overlying organic films,[83] in this work no special precautions have been taken to assemble devices with a specific structure of self-assembled monolayers or of additional passivation layers. If ever done, an additional rigorous study would then need to replicate all experiments (GIWAXS, XRR, and AFM) in the new systems.

Work can be anticipated in the direction of optimizing the solution processability of the F3 and F7 derivatives and extending this synthetic strategy to PDI-based polyfluorinated species. Indeed, as further lowering of their LUMO levels and narrowing their band gaps are in these cases expected, additional functional properties may arise, such as increased charge mobility and bright electro- or photoinduced luminescence.

ASSOCIATED CONTENT

Supporting Information

The Supporting Information is available free of charge at https://pubs.acs.org/doi/10.1021/acsomega.3c05172.

UV-vis absorption spectra of F0, F3, F5 and F7 in 1,4-dioxane solution (Figure S1); FT-IR absorption spectra of F0, F3, F5 and F7 in KBr pellets (Figure S2); NMR spectra of F3, F5 and F7 in DMSO (Figure S3); XRD characterization of F3 and F7 films (Figure S4); contact angle determination of sessile water droplets deposited on pressed pellets of F3, F5 and F7 (Figure S5); GIWAXS images for F3, F5, and F7 (Figures S6 and S7). Determination of the thickness of highly oriented polycrystalline F5 films (Figure S8); AFM characterization of the F5 film (Figure S9); XRD characterization of F5 films (Figure S10, S11 and S12). Comparative structural analysis (Figure S13). OTFT characteristics of the F5 film (Figure S14) (PDF)

AUTHOR INFORMATION

Corresponding Authors

Silvia Milita − *Istituto per la Microelettronica e Microsistemi, Consiglio Nazionale delle Ricerche, 40129 Bologna, Italy;* orcid.org/0000-0002-9612-2541; Email: milita@bo.imm.cnr.it

Antonietta Guagliardi − *Istituto di Cristallografia and To.Sca.Lab, Consiglio Nazionale delle Ricerche, 22100 Como, Italy;* orcid.org/0000-0001-6390-2114; Email: antonella.guagliardi@ic.cnr.it

Norberto Masciocchi − *Department of Science and High Technology and To.Sca.Lab, University of Insubria and INSTM, 22100 Como, Italy;* orcid.org/0000-0001-9921-2350; Email: norberto.masciocchi@uninsubria.it

Authors

Marco Zambra − *Department of Science and High Technology and To.Sca.Lab, University of Insubria and INSTM, 22100 Como, Italy;* orcid.org/0000-0002-9800-8902

Vincenzo Mirco Abbinante − *Department of Science and High Technology and To.Sca.Lab, University of Insubria and INSTM, 22100 Como, Italy;* orcid.org/0000-0002-2918-9324

Gonzalo García-Espejo − *Department of Science and High Technology and To.Sca.Lab, University of Insubria and INSTM, 22100 Como, Italy;* Present Address: Departamento de Qumica Inorgánica, Universidad de Granada, Av. Fuentenueva s/n, 18071 Granada, Spain; orcid.org/0000-0002-2545-1954

Konstantis F. Konidaris − *Department of Science and High Technology and To.Sca.Lab, University of Insubria and INSTM, 22100 Como, Italy;* orcid.org/0000-0002-7366-5682

Pietro Anzini − *Department of Science and High Technology and To.Sca.Lab, University of Insubria and INSTM, 22100 Como, Italy;* orcid.org/0000-0001-9065-9236

Candida Pipitone − *Dipartimento di Fisica e Chimica "Emilio Segrè", Università di Palermo, 90128 Palermo, Italy*

Francesco Giannici − *Dipartimento di Fisica e Chimica "Emilio Segrè", Università di Palermo, 90128 Palermo, Italy;* orcid.org/0000-0003-3086-956X

https://doi.org/10.1021/acsomega.3c05172
ACS Omega 2023, 8, 43651−43663

Mattia Scagliotti − *Istituto per la Microelettronica e Microsistemi - Consiglio Nazionale delle Ricerche, 00133 Roma, Italy;* orcid.org/0000-0001-8505-6377
Matteo Rapisarda − *Istituto per la Microelettronica e Microsistemi - Consiglio Nazionale delle Ricerche, 00133 Roma, Italy;* orcid.org/0000-0002-2629-3855
Luigi Mariucci − *Istituto per la Microelettronica e Microsistemi - Consiglio Nazionale delle Ricerche, 00133 Roma, Italy;* orcid.org/0000-0003-1872-0009

Complete contact information is available at: https://pubs.acs.org/10.1021/acsomega.3c05172

Author Contributions

The manuscript was written through contributions of all authors. All authors have given approval to the final version of the manuscript.

Funding

This project was partially supported by MIUR (PRIN-2017, Project 2017L8WW48, HY-TEC).

Notes

The authors declare no competing financial interest.

■ ACKNOWLEDGMENTS

The authors thank the Italian Ministry of Research for partial funding (Project PRIN 2017L8WW48, HY-TEC. Hybrid ThermoElectric Composites: Proof-of-concepts for low-*T*, n-type, and flexible thermoelectrics) and the University of Insubria for a Junior Assignee Grant.

■ REFERENCES

(1) Cicoira, F.; Santato, C., Eds.; *Organic Electronics: Emerging Concepts and Technologies*; Wiley: New York, USA, 2013.
(2) Ogawa, S., Ed.; *Organic Electronics Materials and Devices*; Springer: Tokyo, Japan, 2015.
(3) Logothetidis, S., Ed.; *Handbook of Flexible Organic Electronics, Materials, Manufacturing and Applications*; Woodhead Pub Ltd: Sawston, UK, 2014.
(4) Brédas, J. L.; Marder, S. R., Eds., *The WSPC Reference on Organic Electronics: Organic Semiconductors*; World Scientific Publishing: Singapore, 2016.
(5) Cosseddu, P.; Caironi, M., eds.; *Organic Flexible Electronics: Fundamentals, Devices, and Applications*, 1st ed.; Woodhead Pub Ltd.: Sawston, UK, 2020.
(6) Bonassieux, Y.; et al. The 2021 flexible and printed electronics roadmap. *Flex. Print. Electr.* **2022**, *6*, No. 023001.
(7) Tao, M.; Hamada, H.; Druffel, T.; Lee, J.-J.; Rajeshwa, K. Research Needs for Photovoltaics in the 21st Century. *ECS J. Solid State Sci. Techn.* **2020**, *9*, 125010.
(8) Dhar, J.; Salzner, U.; Patil, S. Trends in molecular design strategies for ambient stable n-channel organic field effect transistors. *J. Mater. Chem. C* **2017**, *5*, 7404−7430.
(9) Nikolka, M. A perspective on overcoming water-related stability challenges in molecular and hybrid semiconductors. *MRS Commun.* **2020**, *10*, 98−111.
(10) Griggs, S.; Marks, A.; Bristow, H.; McCulloch, I. n-Type organic semiconducting polymers: stability limitations, design considerations and applications. *J. Mater. Chem. C* **2021**, *9*, 8099−8128.
(11) Diao, Y.; Shaw, L.; Bao, Z.; Mannsfed, S. C. B. Morphology control strategies for solution-processed organic semiconductor thin films. *Energy Environ. Sci.* **2014**, *7*, 2145−2159.
(12) Dimitrakopoulos, C. D.; Mascaro, D. J. Organic thin-film transistors: A review of recent advances. *IBM J. Res. Dev.* **2001**, *45*, 11−27.
(13) Sakai, N.; Mareda, J.; Vauthey, E.; Matile, S. Core-substituted naphthalenediimides. *Chem. Commun.* **2010**, *46*, 4225−4237.
(14) Al Kobaisi, M.; Bhosale, S. V.; Latham, K.; Raynor, A. M.; Bhosale, S. V. Functional Naphthalene Diimides: Synthesis, Properties, and Applications. *Chem. Rev.* **2016**, *116*, 11685−11796.
(15) Kumar, S.; Shukla, J.; Kumar, J.; Mukhopadhyay, P. Electron-Poor Arylenediimides. *Org. Chem. Front.* **2018**, *5*, 2254−2276.
(16) Zhang, D.; Zhaob, L.; Zhua, Y.; Lia, A.; Hea, C.; Yub, H.; Hea, Y.; Yana, C.; Gotoa, O.; Menga, H. Effects of *p*-(trifluoromethoxy)-benzyl and *p*- (trifluoromethoxy)phenyl Molecular Architecture on the Performance of Naphthalene Tetracarboxylic Diimide Based Air Stable n-Type Semiconductors. *ACS Appl. Mater. Interfaces* **2016**, *8*, 18277−18283.
(17) Clikeman, T. T.; Bukovsky, E. V.; Wang, X.-B.; Chen, Y.-S.; Rumbles, G.; Strauss, S. H.; Boltalina, O. V. Core Perylene Diimide Designs via Direct Bay- and *ortho*-(Poly)- trifluoromethylation: Synthesis, Isolation, X-ray Structures, Optical and Electronic Properties. *Eur. J. Org. Chem.* **2015**, *30*, 6641−6654.
(18) Guo, X.; Facchetti, A.; Marks, T. J. Imide- and Amide-Functionalized Polymer Semiconductors. *Chem. Rev.* **2014**, *114*, 8943−9021.
(19) Marin, F.; Zappi, A.; Melucci, D.; Maini, L. Self-organizing maps as a data-driven approach to elucidate the packing motifs of perylene diimide derivatives. *Mol. Syst. Des. Eng.* **2023**, *8*, 500−515.
(20) Ruiz Delgado, M. C.; Kim, E.-G.; DaSilva Filho, D. A.; Brédas, J.-L. Tuning the Charge-Transport Parameters of Perylene Diimide Single Crystals via End and/or Core Functionalization: A Density Functional Theory Investigation. *J. Am. Chem. Soc.* **2010**, *132*, 3375−3387.
(21) Vura-Weis, J.; Ratner, M. A.; Wasielewski, M. R. Geometry and Electronic Coupling in Perylenediimide Stacks: Mapping Structure−Charge Transport Relationships. *J. Am. Chem. Soc.* **2010**, *132*, 1738−1739.
(22) Shukla, D.; Nelson, S. F.; Freeman, D. C.; Rajeswaran, M.; Ahearn, W. G.; Meyer, D. M.; Carey, J. T. Thin-Film Morphology Control in Naphthalene-Diimide-Based Semiconductors: High Mobility n-Type Semiconductor for Organic Thin-Film Transistors. *Chem. Mater.* **2008**, *20*, 7486−7491.
(23) Cowen, L. M.; Atoyo, J.; Carnie, M. J.; Baran, D.; Schroeder, B. C. Organic Materials for Thermoelectric Energy Generation. *ECS J. Solid State Sci. Technol.* **2017**, *6*, N3080−N3088.
(24) Russ, B.; Robb, M. J.; Brunetti, F. G.; Levi Miller, P.; Perry, E. E.; Patel, S. N.; Ho, V.; Chang, W. B.; Urban, J. J.; Chabinyc, M. L.; Hawker, C. J.; Segalman, R. A. Power Factor Enhancement in Solution-Processed Organic n-Type Thermoelectrics Through Molecular Design. *Adv. Mater.* **2014**, *26*, 3473−3477.
(25) Cowen, L. M.; Gilhooly-Finn, P. A.; Giovannitti, A.; LeCroy, G.; Demetriou, H.; Neal, W.; Dong, Y.; Westwood, M.; Luong, S.; Fenwick, O.; Salleo, A.; Heutz, S.; Nielsen, C. B.; Schroeder, B. C. Critical analysis of self-doping and water-soluble n-type organic semiconductors: structures and mechanisms. *J. Mater. Chem. C* **2022**, *10*, 8955−8963.
(26) Liscio, F.; Milita, S.; Albonetti, C.; D'Angelo, P.; Guagliardi, A.; Masciocchi, N.; Della Valle, R. G.; Venuti, E.; Brillante, A.; Biscarini, F. Structure and Morphology of PDI8-CN2 for n-Type Thin-Film Transistors. *Adv. Funct. Mater.* **2012**, *22*, 943−953.
(27) Ferlauto, L.; Liscio, F.; Orgiu, E.; Masciocchi, N.; Guagliardi, A.; Biscarini, F.; Samorì, P.; Milita, S. Enhancing the Charge Transport in Solution-Processed Perylene Di-imide Transistors via Thermal Annealing of Metastable Disordered Films. *Adv. Funct. Mater.* **2014**, *24*, 5503−5510.
(28) Milita, S.; Liscio, F.; Cowen, L.; Cavallini, M.; Drain, B. A.; Degousée, T.; Luong, S.; Fenwick, O.; Guagliardi, A.; Schroeder, B. C.; Masciocchi, N. Polymorphism in N,N'-dialkyl-naphthalenediimides. *J. Mater. Chem. C* **2020**, *8*, 3097−3112.
(29) Abbinante, V. M.; García-Espejo, G.; Calabrese, G.; Milita, S.; Barba, L.; Marini, D.; Pipitone, C.; Giannici, F.; Guagliardi, A.; Masciocchi, N. Conformationally rigid molecular and polymeric

naphthalene-diimides containing $C_6H_6N_2$ constitutional isomers. *J. Mater. Chem. C* **2021**, *9*, 10875−10888.
(30) Abbinante, V. M.; Zambra, M.; García-Espejo, G.; Pipitone, C.; Giannici, F.; Milita, S.; Guagliardi, A.; Masciocchi, N. Molecular design and crystal chemistry of polyfluorinated naphthalene-bis-hydrazimides. *Chem. − Eur. J.* **2023**, *29*, No. e202203441.
(31) Sun, H.; Gerasimov, J.; Berggren, M.; Fabiano, S. n-Type organic electrochemical transistors: materials and challenges. *J. Mater. Chem. C* **2018**, *6*, 11778−11784.
(32) Katz, H. E.; Siegrist, T.; Schön, J. H.; Kloc, Ch.; Batlogg, B.; Lovinger, A. J.; Johnson, J. Solid-State Structural and Electrical Characterization of N-Benzyl and N-Alkyl Naphthalene 1,4,5,8-Tetracarboxylic Diimides. *ChemPhysChem* **2001**, *2*, 167−172.
(33) Zhao, L.; Zhang, D.; Zhu, Y.; Peng, S.; Meng, H.; Huang, W. Effects of a highly lipophilic substituent on the environmental stability of naphthalene tetracarboxylic diimide-based n-channel thin-film transistors. *J. Mater. Chem. C* **2017**, *5*, 848−853. and references therein
(34) He, F.; Jin, K.; Wang, J.; Luo, Y.; Sun, J.; Fang, Q. New Fluoropolymers Having Both Low Water Uptake and a Low Dielectric Constant. *Macrom. Chem. Phys.* **2015**, *23*, 2202−2308.
(35) Babudri, F.; Farinola, G. M.; Naso, F.; Ragni, R. Fluorinated organic materials for electronic and optoelectronic applications: the role of the fluorine atom. *Chem. Commun.* **2007**, *10*, 1003−1022.
(36) Ge, Z.; Yang, S.; Tao, Z.; Liu, J.; Fan, L. Synthesis and Characterization of Novel Soluble Fluorinated Aromatic Polyamides Derived from Fluorinated Isophthaloyl Dichlorides and Aromatic Diamines. *Polymer* **2004**, *45*, 3627−3635.
(37) Chen, H.-Z.; Shi, M.-M.; Aernouts, T.; Wang, M.; Borghs, G.; Heremans, P. A Novel Organic N-Type Material: Fluorinated Perylene Diimide. *Sol. Energy Mater. Sol. Cells* **2005**, *87*, 521−527.
(38) Hou, Y.; Chen, G.; Pei, X.; Fang, X. Synthesis and Characterization of Novel Optically Transparent and Organosoluble Polyimides Based on Diamines Containing Cyclohexane Moiety. *J. Polym. Res.* **2012**, *19* (9), 9955.
(39) Lemal, D. M. Perspective on fluorocarbon chemistry. *J. Org. Chem.* **2004**, *69*, 1−11.
(40) Bowman, J. S. Fluorotechnology is critical to modern life: the FluoroCouncil counterpoint to the Madrid Statement. *Environ. Health Persp.* **2015**, *123*, A112−113.
(41) Ajayakumar, M. R.; Mukhopadhyay, P. Naphthalene-bis-hydrazimide: radical anions and ICT as new bimodal probes for differential sensing of a library of amine. *Chem. Commun.* **2009**, *25*, 3702−3704.
(42) Ajayakumar, M. R.; Mukhopadhyay, P.; Yadav, S.; Ghosh, S. Single-Electron Transfer Driven Cyanide Sensing: A New Multimodal Approach. *Org. Lett.* **2010**, *12*, 2646−2649.
(43) Frisch, M. J.; Trucks, G. W.; Schlegel, H. B.; Scuseria, G. E.; Robb, M. A.; Cheeseman, J. R.; Scalmani, G.; Barone, V.; Petersson, G. A.; Nakatsuji, H.; Li, X.; Caricato, M.; Marenich, A. V.; Bloino, J.; Janesko, B. G.; Gomperts, R.; Mennucci, B.; Hratchian, H. P.; Ortiz, J. V.; Izmaylov, A. F.; Sonnenberg, J. L.; Williams-Young, D.; Ding, F.; Lipparini, F.; Egidi, F.; Goings, J.; Peng, B.; Petrone, A.; Henderson, T.; Ranasinghe, D.; Zakrzewski, V. G.; Gao, J.; Rega, N.; Zheng, G.; Liang, W.; Hada, M.; Ehara, M.; Toyota, K.; Fukuda, R.; Hasegawa, J.; Ishida, M.; Nakajima, T.; Honda, Y.; Kitao, O.; Nakai, H.; Vreven, T.; Throssell, K.; Montgomery, J. A., Jr.; Peralta, J. E.; Ogliaro, F.; Bearpark, M. J.; Heyd, J. J.; Brothers, E. N.; Kudin, K. N.; Staroverov, V. N.; Keith, T. A.; Kobayashi, R.; Normand, J.; Raghavachari, K.; Rendell, A. P.; Burant, J. C.; Iyengar, S. S.; Tomasi, J.; Cossi, M.; Millam, J. M.; Klene, M.; Adamo, C.; Cammi, R.; Ochterski, J. W.; Martin, R. L.; Morokuma, K.; Farkas, O.; Foresman, J. B.; Fox, D. J. *Gaussian 16, Revision C.01*; Gaussian, Inc.: Wallingford CT, 2016.
(44) Becke, A. D. Density-functional thermochemistry. III. The role of exact exchange. *J. Chem. Phys.* **1993**, *98*, 5648−5652.
(45) Stephens, P. J.; Devlin, F. J. M.; Chabalowski, C. F.; Frisch, M. J. Ab Initio Calculation of Vibrational Absorption and Circular Dichroism Spectra Using Density Functional Force Fields. *J. Chem. Phys.* **1994**, *98*, 11623−11627.
(46) Adamo, C.; Jacquemin, D. The calculations of excited-state properties with Time-Dependent Density Functional Theory. *Chem. Soc. Rev.* **2013**, *42*, 845−856.
(47) Martin, R. L. Natural transition orbitals. *J. Chem. Phys.* **2003**, *118*, 4775−4777.
(48) Lamour, G.; Hamraoui, A.; Buvailo, A.; Xing, Y.; Keuleyan, S.; Prakash, V.; Eftekhari-Bafrooei, A.; Borguet, E. Contact Angle Measurements Using a Simplified Experimental Setup. *J. Chem. Educ.* **2010**, *87*, 1403−1407.
(49) Stalder, A. R.; Melchior, T.; Muller, M.; Sage, D.; Blu, T.; Unser, M. Low-Bond Axisymmetric Drop Shape Analysis for Surface Tension and Contact Angle Measurements of Sessile Drops. *Colloids Surf., A* **2010**, *364*, 72−81.
(50) Schrode, B.; Pachmajer, S.; Dohr, M.; Röthel, C.; Domke, J.; Fritz, T.; Resel, R.; Werzer, O. GIDVis: A Comprehensive Software Tool for Geometry-Independent Grazing-Incidence X-Ray Diffraction Data Analysis and Pole-Figure Calculations. *J. Appl. Crystallogr.* **2019**, *52*, 683−689.
(51) *Version 2.1*; Rigaku Corp.: Tokyo, Japan, 2009.
(52) Kainz, M. P.; Legenstein, L.; Holzel, V.; Hofel, S.; Kaltenergger, M.; Resel, R.; Simbrunner, J. GIDInd: an automated indexing software for grazing-incidence X-ray diffraction data. *J. Appl. Crystallogr.* **2021**, *54*, 1256−1267.
(53) *TOPAS-R, V. 3.0*; Bruker AXS: Karlsruhe, Germany, 2005.
(54) Facchetti, A. Semiconductors for organic transistors. *Mater. Today* **2007**, *10*, 28−37.
(55) Park, J. W.; Kang, B. H.; Kim, H. J. A Review of Low-Temperature Solution-Processed Metal Oxide Thin-Film Transistors for Flexible Electronics. *Adv. Funct. Mater.* **2020**, *30*, No. 1904632.
(56) Viola, F. A.; Barsotti, J.; Melloni, F.; Lanzani, G.; Kim, Y.-H.; Mattoli, V.; Caironi, M. A sub-150-nanometre-thick and ultra-conformable solution-processed all-organic transistor. *Nat. Commun.* **2021**, *12*, 5842.
(57) Vazquez-Mena, O.; Gross, L.; Xie, S.; Villanueva, L. G.; Brugger, J. Resistless nanofabrication by stencil lithography: A review. *Microelectr. Eng.* **2015**, *132*, 236−254.
(58) Ajayakumar, M. R.; Hundal, G.; Mukhopadhyay, P. A tetrastable naphthalenediimide: anion induced charge transfer, single and double electron transfer for combinational logic gates. *Chem. Commun.* **2013**, *49*, 7684−7686.
(59) Gosztola, D.; Niemczyk, M. P.; Svec, W.; Lukas, A. S.; Wasielewski, M. R. Excited Doublet States of Electrochemically Generated Aromatic Imide and Diimide Radical Anions. *J. Phys. Chem. A* **2000**, *104*, 6545−6551.
(60) Wang, J.; He, E.; Liu, X.; Yu, L.; Wang, H.; Zhang, R.; Zhang, H. High performance hydrazine vapor sensor based on redox mechanism of twisted perylene diimide derivative with lower reduction potential. *Sens. Actuators, B* **2017**, *239*, 898−905.
(61) Sarma, N. S.; Sarma, S.; Gogoi, G.; Bhattacharya, L.; Sahoo, S. R.; Sahu, S. Enhancement of air-stability, π-stacking ability, and charge transport properties of fluoroalkyl side chain engineered n-type naphthalene tetracarboxylic diimide compounds. *RSC Adv.* **2021**, *11*, 57−70.
(62) Taylor, M.; Urquhart, A. J.; Zelzer, M.; Davies, M. C.; Alexander, M. R. Picoliter Water Contact Angle Measurement on Polymers. *Langmuir* **2007**, *23*, 6875−6878.
(63) Ruiz Delgado, M. C.; Kim, F. G.; da Silva Filho, D. A.; Brédas, J. L. Tuning the Charge-Transport Parameters of Perylene Diimide Single Crystals via End and/or Core Functionalization: A Density Functional Theory Investigation. *J. Am. Chem. Soc.* **2010**, *132*, 3375−3387.
(64) Shukla, J.; Mukhopadhyay, P. Synthesis of Functionalized Naphthalene Diimides and their Redox Properties. *Eur. J. Org. Chem.* **2019**, *2019*, 7770−7786.
(65) McCormick, T. M.; Bridges, C. R.; Carrera, E. I.; DiCarmine, P. M.; Gibson, G. L.; Hollinger, J.; Kozycz, L. M.; Seferos, D. S. Conjugated Polymers: Evaluating DFT Methods for More Accurate Orbital Energy Modeling. *Macromolecules* **2013**, *46*, 3879−3886.

https://doi.org/10.1021/acsomega.3c05172
ACS Omega 2023, 8, 43651−43663

(66) Zhan, C. G.; Nichols, J. A.; Dixon, D. A. Ionization Potential, Electron Affinity, Electronegativity, Hardness, and Electron Excitation Energy: Molecular Properties from Density Functional Theory Orbital Energies. *J. Phys. Chem. A* **2003**, *107*, 4184−4195.
(67) Sworakowski, J.; Lipiński, J.; Janus, K. On the reliability of determination of energies of HOMO and LUMO levels in organic semiconductors from electrochemical measurements. A simple picture based on the electrostatic model. *Org. Electr.* **2016**, *33*, 300−310.
(68) Park, S. K.; Kim, J. H.; Park, S. Y. Organic 2D Optoelectronic Crystals: Charge Transport, Emerging Functions, and Their Design Perspective. *Adv. Mater.* **2018**, *30*, No. 1704759.
(69) Dollase, W. A. Correction of intensities for preferred orientation in powder diffractometry: application of the March model. *J. Appl. Crystallogr.* **1986**, *19*, 267−272.
(70) Rapisarda, M.; Valletta, A.; Daami, A.; Jacob, S.; Benwadih, M.; Coppard, R.; Fortunato, G.; Mariucci, L. Analysis of contact effects in fully printed p-channel organic thin film transistors. *Org. Electron.* **2012**, *13*, 2017−2027.
(71) Facchetti, A. Semiconductors for organic transistors. *Mater. Today* **2007**, *10*, 28−37.
(72) Viola, F. A.; Barsotti, J.; Melloni, F.; Lanzani, G.; Kim, Y.-H.; Mattoli, V.; Caironi, M. A sub-150-nanometre-thick and ultra-conformable solution-processed all-organic transistor. *Nat. Commun.* **2021**, *12*, 5842.
(73) Vazquez-Mena, O.; Gross, L.; Xie, S.; Villanueva, L. G.; Brugger, J. Resistless nanofabrication by stencil lithography: A review. *Microelectr. Eng.* **2015**, *132*, 236−254.
(74) Zaumseil, J.; Sirringhaus, H. Electron and ambipolar transport in organic field-effect transistors. *Chem. Rev.* **2007**, *107*, 1296−1323.
(75) Katz, H. E.; Lovinger, A. J.; Johnson, J.; Kloc, C.; Siegrist, T.; Li, W.; Lin, Y.-Y.; Dodabalapur, A. A soluble and air-stable organic, semiconductor with high electron mobility. *Nature* **2000**, *404*, 478−481.
(76) Chlebosz, D.; Goldeman, W.; Janus, K.; Szuster, M.; Kiersnovski, A. Synthesis, Solution, and Solid State Properties of Homological Dialkylated Naphthalene Diimides — A Systematic Review of Molecules for Next-Generation Organic Electronics. *Molecules* **2023**, *28*, 2940.
(77) Singh, M.; Kaur, N.; Comini, E. The role of self-assembled monolayers in electronic devices. *J. Mater. Chem. C* **2020**, *8*, 3938−4055.
(78) Dash, T.; Palei, B. B.; Dash, B.; Sahu, R. K.; Moharana, R. K.; Dhar, S.; Biswal, S. K. Graphene reinforced silicon composites and their characterizations. *Mater. Today: Proc.* **2022**, *62*, 5962−5964.
(79) Simeone, D.; Cipolloni, S.; Mariucci, L. M.; Rapisarda, M.; Minotti, A.; Pecora, A.; Cuscunà, M.; Maiolo, L.; Fortunato, G. Pentacene TFTs with parylene passivation layer. *Thin Solid Films* **2011**, *517*, 6283−6286.
(80) Jeong, E. G.; Kwon, J. H.; Kang, K. S.; Jeong, E. G.; Choi, K. C. A review of highly reliable flexible encapsulation technologies towards rollable and foldable OLEDs. *J. Inf. Dispersion* **2020**, *21*, 19−32. and references therein
(81) Rapisarda, M.; Simeone, D.; Fortunato, G.; Valletta, A.; Mariucci, L. Pentacene thin film transistors with (polytetrafluoro-ethylene) PTFE-like encapsulation layer. *Org. Electron.* **2011**, *12*, 119−124.
(82) Hansch, C.; Leo, A.; Unger, S. H.; Kim, K. H.; Nikaitani, D.; Lien, E. J. Aromatic substituent constants for structure-activity correlations. *J. Med. Chem.* **1973**, *16*, 1207−1216.
(83) Scavia, G.; Porzio, W.; Destri, S.; Barba, L.; Arrighetti, G.; Milita, S.; Fumagalli, L.; Natali, D.; Sampietro, M. Effect of the silanization and annealing on the morphology of thin poly(3-hexylthiophene) (P3HT) layer on silicon oxide. *Surf. Sci.* **2008**, *602*, 3106−3115.

https://doi.org/10.1021/acsomega.3c05172
ACS Omega 2023, 8, 43651−43663